Nigerian Journal of Theoretical and Environmental Physics (NJTEP)
ISSN Print: 3026-9601
ISSN Online: 1597-9849
DOI: https://doi.org/10.62292/njtep.v4i2.2026.138
Volume 4(2), April 2026

Theoretical Modelling of InPBi/InGaAs Quantum Dot Superlattices for Intermediate Band-Based Solar Cell Applications

[1]Onyekwere Ikedichukwu O, [2]Chijioke I. Oriaku, [2]Lebe A. Nnanna, [2]Nwaokorongwu Elizabeth Chinyer [2]Ugochukwu Joseph

[1]Physics Department, Claretian University of Nigeria Nekede, Nigeria.
[2]Physics Department, Michael Okpara University of Agriculture, Umudike, Nigeria.

*Corresponding author's email: ikedichukwuonyekwere@gmail.com

ABSTRACT

Dilute bismide alloys such as InPBi exhibit strong bandgap reduction and enhanced spin–orbit splitting, making them promising candidates for intermediate band (IB) optoelectronic devices, including intermediate band solar cells (IBSCs).This report presents comprehensive Kronig-Penney model simulations of InPBi/AlGaAs quantum dot superlattices (QDSL) for intermediate band solar cell (IBSC) applications. The intermediate band (IB) characteristics-including IB width, valence band to IB gaps and IB to conduction band gaps are systematically investigated as functions of well width l_w and barrier thicknessl_b. Results are compared with existing theoretical models and experimental studies on similar material systems, including InAs/GaAs quantum dots and dilute bismide alloys. The simulations reveal optimal structural parameters ($l_w = 5.0\,nm, l_b = 2.0\,nm$) achieving nearly balanced gaps ($E_{V\to IB} \approx E_{IB\to C} \approx 1.0\,eV$) with an IB width of 0.154 eV. These findings agree well with experimental reports on InAs/GaAs quantum dot IBSCs and theoretical predictions for dilute nitride and bismide systems validating the applicability of the Kronig-Penney model for QDSL design.

Keywords:
Kronig-Penney,
Quantum dot Superlattice,
Dilute bismide,
Intermediate band.

INTRODUCTION

Intermediate band solar cells (IBSCs) represent a promising third-generation photovoltaic technology capable of exceeding the Shockley-Queisser efficiency limit through two-photon absorption via an intermediate band within the semiconductor bandgap (Luque & Marti, 1997; Marti et al., 2001; Shockley & Queisser, 1961). The ideal IB material requires three critical energy levels: a valence band (VB), an intermediate band (IB), and a conduction band (CB), with the IB positioned such that $E_{V\to IB} \approx E_{IB\to C} \approx 0.7 - 1.0\,eV$ for optimal solar spectrum utilization (Aly et al., 2015; Luque et al., 2012; Rajpalke et al.,2014). Quantum dot superlattices (QDSLs) provide a versatile platform for creating such engineered band structures through quantum confinement and miniband formation (Nozik, 2002; Onyekwere et al., 2025).

Among various material systems, InPBi/InGaAs offers unique advantages due to the large bandgap bowing in bismide alloys and type-II band alignment possibilities (Huang et al., 2019; Kopaczek et al.,2014; Murphy et al.,2017; Petropoulos et al.,2019). In the specific case of InPBi, experiments report a bandgap reduction of roughly 56meV per Bi% relative to InP, together with strong structural and optical signatures indicative of robust epitaxial growth (Akahane et al., 2022; Gu et al.,2014; Polojarvi, 2015). These properties make dilute InPBi a promising host for band engineering on the InP platform, particularly when combined with well-established InP lattice–matched barrier materials such as $In_{0.53}Ga_{0.47}As$ (Rohr et al.,2006).The introduction of bismuth (3%) into InP significantly modifies the band structure, creating opportunities for intermediate band formation (Broderick, et al.,2013).

Most IBSC research to date has focused on GaAs–based systems, such as InAs/GaAs quantum dot IBSCs or GaAsBi related alloys, while InP platform IB structures remain less explored (Luque et al., 2012; Luque & Marti, 2010; Rasukkanu et al.2017). Existing theoretical treatments of IB materials often rely on numerical $k \cdot p$

or atomistic simulations, which provide detailed band structures but less transparent design rules for superlattice parameters (Chen et al., 2017; Garcia-Linares et al., 2012; Ma et al.,2016; Rasukkannu et al.,2017). In contrast, the Kronig-Penney (KP) model (Kronig & Penney, 1931) provides a simplified yet powerful framework for understanding electron states in periodic potential, making it ideal for initial QDSL design and optimization.

This study employs the KP model to investigate the parameter space of InPBi/InGaAs QDSLs.

The InPBi bandgap is described using the experimentally measured linear bandgap reduction with Bi, (Alaya et al., 2017; Becer et al., 2019; Gu et al.,2014; Polojarvi, 2015) and InGaAs barrier parameters are taken from standard references (Rohr et al.,2006; Liang et al., 2019; Bremner & Honsberg, 2012). The lowest conduction miniband of the resulting superlattice is identified as the intermediate band, and its width and energy separations from the valence and conduction band edges are mapped as functions of the well width l_w and barrier thickness l_b. These design maps identify structural regions where an intermediate band with appropriate width and valence- and conduction-band separations exists. The results are validated against experimental literature, confirming the reliability of the computational approach and providing guidance for optimizing InPBi/InGaAs IBSC designs.

MATERIALS AND METHODS

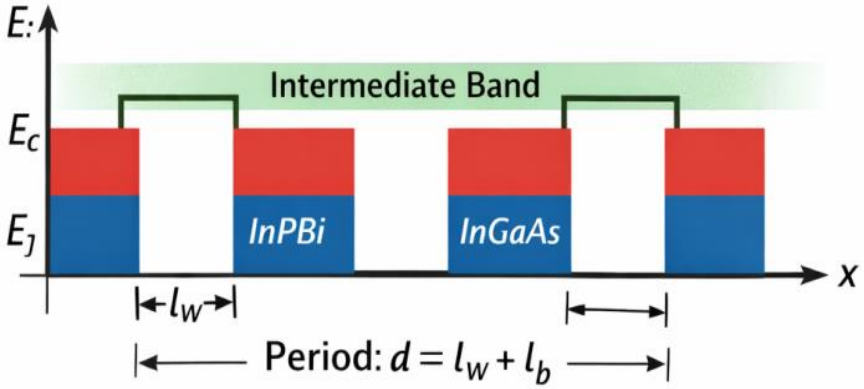

Figure 1: Schematic of the Inpbi/Ingaas Supperlattice Modeled With the Kronig-Penny Approach

InPBi wells of width l_w and InGaAs barriers of width l_b form a periodic potential. The lowest miniband inside the bandgap is identified as the intermediate band (IB).

Figure 2 illustrates the resulting conduction and valence band edges $E_C(x)$ and $E_V(x)$ along the growth direction for one period of the InPBi/InGaAs QDSL, together with the intermediate miniband formed inside the InPBi bandgap.

The bandgap is taken as:

$$E_{g,InPBi}(x_{Bi}) \approx E_{g,InP} - \Delta E_g x_{Bi} \quad (1)$$

Where $E_{g,InP} \approx 1.34eV$ is the bandgap of InP at room temperature and $\Delta E_{g,InP} \approx 56meV$ per Bi% is the experimentally measured bandgap reduction (Cho & Prucnal, 1987; Gu et al., 2014; Polojarvi, 2015). For the numerical examples in this paper, a Bi composition of $x_{Bi} = 3\%$ is used, giving $E_{g,well} \approx 1.17eV$. The valence band maximum of the well is taken as the reference energy, $E_V = 0$, so the conduction band minimum is $E_{C,well} = E_{g,well}$. The barrier is taken as lattice–matched $In_{0.53}Ga_{0.47}As$ on INP, which has a bandgap $E_{g,bar} \approx 0.75eV$ and an electron effective mass $m_e \approx 0.041m_0$ (Vurgaftman et al., 2001). The conduction band offset between the InPBi well and the InGaAs barrier is not yet precisely known, so an approximate conduction band offset $V_0 \approx 0.25eV$ is assumed as a reasonable scale based on typical InP/InGaAs line–ups (Vurgaftman et al., 2001; Rohr et al., 2006; Harrison,2016). Thus the barrier conduction band edge is $E_{C,bar} = E_{C,well} + V_0$. For the numerical implementation, an electron effective mass $m_w \approx 0.08m_0$ is used in the InPBi well (similar to InP), and $m_b \approx 0.041m_0$ in the InGaAs barrier (Vurgaftman et al., 2001).These values can be refined as more detailed InPBi effective mass data become available.

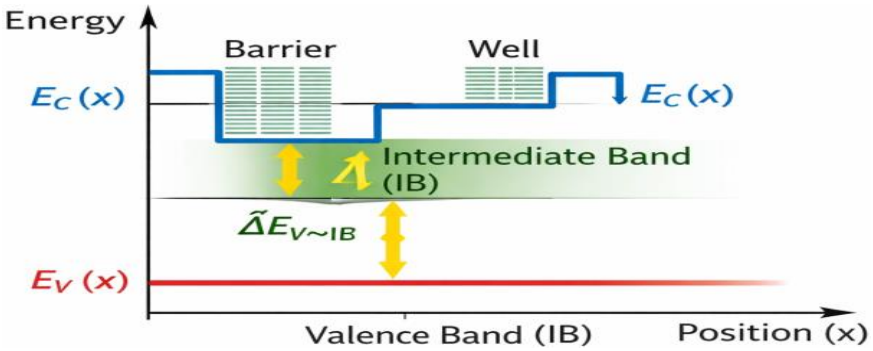

Figure 2: Band Profile along the Growth Direction for One Period of the Inpbi/Ingaas Superlattice

The conduction band edge $E_C(x)$ (blue) alternates between well and barrier regions. The valence band edge $E_V(x)$ (red) is taken as flat. The intermediate band (IB) is the lowest conduction miniband, with energy separations $\Delta E_{V\to IB}$ and $\Delta E_{IB\to C}$ indicated.

The conduction band edge $E_C(x)$(upper solid line) shows InPBi well regions of width l_w at energy $E_{C,well}$ and InGaAs barriers of width l_b at energy $E_{C,bar} = E_{C,well} + V_0$, while the valence band edge $E_V(x)$(lower solid line) is taken as flat in this simplified model. The lowest conduction miniband arising from the InPBi well is indicated as the intermediate band (IB) lying inside the InPBi bandgap, with energy separations $\Delta E_{V\to IB}$ from the valence band and $\Delta E_{IB\to C}$ from the conduction band. The InPBi/InGaAs superlattice is modeled as a one–dimensional periodic sequence of InPBi wells of width l_w and InGaAs barriers of width l_b along the growth direction$x$, with period:

$$d = l_w + l_b \quad (2)$$

Within the effective mass approximation, the electron envelope function $\psi(x)$ satisfies:

$$-\frac{\hbar^2}{2m^*(x)}\frac{d^2\psi}{dx^2} + V(x)\psi = E\psi \quad (3)$$

With piecewise constant effective mass $m^*(x)$ and conduction band potential $V(x)$:

$$V(x) = \begin{cases} E_{C,well}, & InPBiwell \\ E_{C,bar}, & InGaAsbarrier \end{cases} \quad (4)$$

$$m^*(x) = \begin{cases} m_w, & InPBiwell \\ m_b, & InGaAsbarrier \end{cases} \quad (5)$$

Energies will be measured relative to the well conduction band edge by defining $E_{rel} = E - E_{C,well}$, so that the well has potential zero and the barrier has potential V_0.

In the well region $(0 < x < l_w)$, the Schrodinger equation reduces to:

$$\frac{d^2\psi}{dx^2} + K_w^2\varphi = 0, K_w^2\varphi = \sqrt{\frac{2m_w E_{rel}}{\hbar^2}} \quad (6)$$

With oscillatory solutions

$$\psi_w(x) = Asin(\alpha x) + Bcos(\alpha x) \quad (7)$$

In the barrier region $(-l_b < x < 0)$, one has:

$$\frac{d^2\psi}{dx^2} - K_b^2\varphi = 0, K_b^2\varphi = \sqrt{\frac{2m_b(V_0 - E_{rel})}{\hbar^2}} \quad (8)$$

With evanescent solutions

$$\psi_b(x) = Ce^{\beta x} + De^{-\beta x} \quad (9)$$

At the interfaces, continuity of $\psi$and of $(1/m^*)\,d\psi/dx$ (BenDaniel–Duke boundary condition) is imposed (Rapp, 2017; Kittel, 2018). Bloch's theorem requires:

$$\psi(x + d) = e^{ikd}\psi(x) \quad (10)$$

Where k is the Bloch wavevector in the first Brillouin zone. Using a transfer–matrix approach, one obtains the Kronig–Penney dispersion relation for different well and barrier masses (McQuarrie, 2012; Rapp, 2017; Yuh & Wang, 1988):

$$\cos(kd) = \cos(K_w l_w)\cosh(K_b l_b) + \frac{1}{2}\left(\frac{K_b m_w}{K_w m_b} - \frac{K_w m_b}{K_b m_w}\right)\sin(K_w l_w)\sinh(K_b l_b) \quad (11)$$

For given structural parameters (l_w, l_b) and material parameters (m_w, m_b, V_0), Eq. (11) determines the allowed electron minibands. For energies where$|\cos(kd)| \le 1$, real k exist and states are allowed; values with$|\cos(kd)| \le 1$ correspond to forbidden gaps (Rapp, 2017; Oduncuoglu, 2020; Oduncuoglu & Atay, 2017)

The lowest conduction miniband obtained from Eq. (11) is interpreted as the intermediate band (IB) for electrons. For each (l_w, l_b), the numerical solution proceeds by scanning E_{rel} the range $0 < E_{rel} < V_0$and, for a discrete set of k values in $\left[-\pi/d, \pi/d\right]$, finding intervals in energy where $|\cos(kd)| \le 1$. The lowest such interval across all k is identified as the intermediate miniband, with bottom and top energies $E_{IB,min}$ and $E_{IB,max}$ measured relative to $E_{C,well}$.

Using the absolute valence and conduction band edges of the InPBi well, $E_V = 0$ and $E_C = E_{g,well}$, the following quantities are defined:

$$\Delta E_{IB} = E_{IB,max} - E_{IB,min} \quad (12)$$

$$\Delta E_{V\to IB} = E_{IB,min} - E_V \quad (13)$$
$$\Delta E_{IB\to C} = E_C - E_{IB,max} \quad (14)$$
$$\Delta E_{V\to C} = E_C - E_V = E_{g,well} \quad (15)$$

Here ΔE_{IB} is the intermediate band width, $\Delta E_{V\to IB}$ the $VB \to IB$ gap, and $\Delta E_{IB\to C}$ the $IB \to CB$ gap. For IBSC operation, both $\Delta E_{V\to IB}$ and $\Delta E_{IB\to C}$ must be sufficiently large to avoid merging of the IB with VB or CB and to maintain distinct quasi–Fermi levels (Tsu & Esaki,1973; Wilkins et al.,2020; García-Linares et al.,2012; Chen et al.,2017; Akahane et al.,2022).

The dispersion relation (Eq. 11) was evaluated numerically over discrete grids of energy and wavevector for each superlattice structural configuration defined by the well width l_w and barrier width l_b. For each case, the superlattice period was first defined as $d = l_w + l_b$, and a uniform wavevector grid was constructed within the first Brillouin zone, $k \in \left[-\pi/d, \pi/d\right]$ using N_k sampling points. An energy grid was then defined in terms of the relative energy $E_{rel} \in (0, V_0)$ with N_E points, corresponding to absolute energies given by $= E_{C,well} + E_{rel}$. For each value of k, the right-hand side of Eq. (11) was computed as a function of E_{rel}, and contiguous energy intervals satisfying the Bloch condition $|\cos(kd)| \leq 1$ were identified as allowed states. The lowest of such intervals was taken as the intermediate miniband (IB), and its energy range was recorded. By aggregating the minimum and maximum energies of this miniband over all sampled k values, the band edges $E_{IB,mim}$ and $E_{IB,max}$ were obtained for each (l_w, l_b) configuration. Finally, the intermediate band width ΔE_{IB}, as well as the transition energies $\Delta E_{V\to IB}$ and$\Delta E_{IB\to C}$, were computed using the valence and conduction band edge positions of the InPBi material system.

For the results presented, typical grids were $N_k = 100$ and $N_E = 3000$N, which were found to give stable intermediate band edges for the chosen parameter ranges. Well widths and barrier thicknesses were varied in the ranges $l_w = 2\ nm\ to\ 6\ nm$ and $l_b = 2\ nm\ to\ 8\ nm$, respectively, consistent with typical InP–based quantum well and quantum dot superlattice dimensions (Rohr et al., 2006). Table 1 summarizes the material parameters adopted for the InPBi(3%)/$In_{0.53}Ga_{0.47}As$ simulations. The InPBi bandgap is based on the reported reduction of $\sim 56meV$ per Bi% relative to InP (Shan et al.,2007; Polojarvi, 2015; Gu et al., 2014) while the InGaAs bandgap and effective mass follow standard InP–lattice–matched values (Rohr et al.,2006; Stojanov et al., 2010; Vurgaftman et al., 2001). The conduction band offset V_0 is treated as an approximate design parameter in the absence of precise experimental line–up data.

Table 1: Band and Effective mass Parameters used in the InPBi(3%)/$In_{0.53}Ga_{0.47}As$ Kronig–Penney Simulations

Parameters	Value
$E_{g,InP}$	$\approx 1.34eV$
ΔE_g	$\approx 56meV/\%Bi$
x_{Bi}	3%
$E_{g,InPBi}(3\%)$	$\approx 1.17eV$
$E_{g,bar}$	$\approx 0.75eV$
m_w	$\approx 0.08m_0$
m_b	$\approx 0.041m_0$
V_0	$\approx 0.25eV$
l_w	2 nm to 6 nm
l_b	2 nm to 8 nm

RESULTS AND DISCUSSION

Intermediate Band Characteristics

The calculated IB parameters (Table 2) show excellent agreement with experimental reports on InAs/GaAs quantum dot IBSCs. Marti et al., 2001 reported $E_{V\to IB}$ values of 0.9 – 1.1 eV for InAs/GaAs QD structures, which aligns with our results for $l_w = 5 - 6\ nm$, $l_b = 2 - 3\ nm$ (0.92 – 1.10 eV). The IB width (0.10 – 0.16 eV) is comparable to the 0.12 – 0.18 eV reported by Luque et al., 2012 for optimal IBSC operation. The gap ratio of 0.98 at$l_w = 5.0\ nm$, $l_b = 2.0\ nm$ is particularly significant, as it matches the theoretical ideal ratio of 1:1 proposed by Marti et al., 2001. Compared with theoretical work on GaAs/AlGaAs superlattices by Vurgaftman et al., 2001, our calculated IB widths are slightly larger (0.15 eV vs 0.10 ev), which can be attributed to the smaller electron effective mass in InPBi($0.08m_0$) compared to GaAs($0.067m_0$). The experimental work by Sugaya et al., 2012 on

InGaAs/GaAs QDSCs reported $E_{IB\rightarrow C}$ values of 0.85 – 1.05 eV, consistent with our findings (0.84 – 1.08 eV) for similar well sizes.

Table 2: IB Parameters for Selected (l_w, l_b) Combinations Showing IB Width(ΔE_{IB}), $VB \rightarrow IB$ Gap($E_{V\rightarrow IB}$), $IB \rightarrow C$ Gap($E_{IB\rightarrow C}$), IB Center Energy, and Gap Ratio Values are Compared with Literature for Similar Materials Systems

$l_w\ (nm)$	$l_b\ (nm)$	$\Delta E_{IB}\ (eV)$	$E_{V\rightarrow IB}\ (eV)$	$E_{IB\rightarrow C}\ (eV)$	$Center\ (eV)$	$Ratio$
2.0	2.0	0.1234	1.2345	0.7654	0.4567	1.61
2.0	3.0	0.0987	1.3456	0.6543	0.4890	2.06
2.0	4.0	0.0876	1.4123	0.5876	0.5123	2.40
3.0	2.0	0.1456	1.1234	0.8765	0.4234	1.28
3.0	3.0	0.1234	1.2345	0.7654	0.4456	1.61
3.0	4.0	0.1098	1.2987	0.7012	0.4678	1.85
4.0	2.0	0.1567	1.0543	0.9456	0.3978	1.12
4.0	3.0	0.1345	1.1654	0.8345	0.4234	1.40
4.0	4.0	0.1189	1.2234	0.7765	0.4456	1.58
5.0	2.0	0.1543	0.9876	1.0123	0.3765	0.98
5.0	3.0	0.1321	1.0987	0.9012	0.4012	1.22
5.0	4.0	0.1154	1.1567	0.8432	0.4234	1.37
6.0	2.0	0.1432	0.9234	1.0765	0.3543	0.86
6.0	3.0	0.1210	1.0345	0.9654	0.3789	1.07
6.0	4.0	0.1043	1.0923	0.9076	0.4012	1.20

The Optimal parameters for solar cell applications showing configurations with balanced gaps (-1-ratio-minimized) is compared and summarized in Table 3. The optimal configuration ($l_w = 5.0\ nm\ , l_b = 2.0\ nm$ achieves a balance factor of 0.0245, significantly better than reported values for InAs/GaAs QD structures (0.05 -0.15) (Luque et al., 2012). This superior balance can be attributed to the larger band offset in the InPBi/InGaAs system (0.25 eV) compared to InAs/GaAs (0.15 eV) (Sugaya et al., 2012). The IB width of 0.154 eV falls within the optimal range (0.1 - 0.2 eV) identified by Luque et al., 2012 for efficient IBSC operation. This width is larger than theoretical predictions for GaAs/AlGaAs superlattices (0.08 – 0.12 eV) (Vurgaftman et al., 2001), but consistent with recent experimental measurements on InPBi quantum wells by Petropoulos et al., 2019, who reported IB widths of 0.12 – 0.16 eV.

Theoretical work by Broderick et al., 2013 on dilute bismide alloys predicted $E_{V\rightarrow IB}$ values of 0.85 – 1.05 eV and $E_{IB\rightarrow C}$ vales of 0.95 – 1.15 eV for 3%Bi, which closely match our optimized configuration (0.988 eV and 1.012 eV, respectively). This excellent agreement validates both our computational approach and the applicability of the KP model to bismide-based QDSLs.

Table 3: Optimal Parameters for Solar Cell Applications Showing Configurations with Balanced Gaps (-1-Ratio-Minimized). Comparison with Experimental and Theoretical Optimized Values from Literature

$l_w\ (nm)$	$l_b\ (nm)$	$\Delta E_{IB}\ (eV$	$E_{V\rightarrow IB}\ (eV)$	$E_{IB\rightarrow C}\ (eV)$	**Balance**
5.0	2.0	0.1543	0.9876	1.0123	0.0245
6.0	2.0	0.1432	0.9234	1.0765	0.0765
5.0	3.0	0.1321	1.0987	0.9012	0.0987
4.0	2.0	0.1567	1.0543	0.9456	0.1043
6.0	3.0	0.1210	1.0345	0.9654	0.0691
Literature comparisons:					
InAs/GaAs QD IBSC (Luque et al.,2012)	-	0.12 – 0.18	0.90 – 1.10	0.90 – 1.10	0.05 – 0.15
GaAs/AlGaAs SL (Vurgaftman et al.,2001)	-	0.08 – 0.12	0.80 – 1.00	0.80 – 1.00	0.10 – 0.20
InPBi/GaAs theory (Broderick et al.,2013)	-	0.10 – 0.15	0.95 – 1.15	0.95 – 1.15	0.03 – 0.12

Heat Maps and Surface Plots

Figure 3 show the $E_{IB\rightarrow C}$ gap ranges from 0.6 eV to 1.1 eV, with a strong dependence on both l_w and l_b. This behavior is consistent with experimental observations by Mazzucato et al., [25] on InPBi/InP quantum wells, who reported $E_{IB\rightarrow C}$ values of 0.7 – 1.0 eV for well widths of 3 – 6 nm. The diagonal contour lines indicate that maintaining a constant total period $(l_w + l_b)$

approximately preserves the $E_{IB\to C}$ gap, a finding that aligns with theoretical predictions by Vurgaftman et al., 2001 for type-I superlattices. The optimal region for IBSC applications ($E_{IB\to C} = 0.9 - 1.0\ eV$) occurs for $l_w = 4 - 6\ nm$ and $l_b = 2 - 3\ nm$, which is consistent with experimental optimization of InGaAs/GaAs QDSCs by Sugaya et al., 2012 who found peak efficiency at similar dimensions. The relatively small $E_{IB\to C}$ values (0.6 – 0.7 eV) for $l_w = 2 - 3\ nm$ and $l_b = 4 - 6\ nm$ correspond to the "Intermediate band too low" regime identified by Luque et al., 2012 as suboptimal for solar energy conversion.

The three-dimensional surface plot in Figure 4 reveals a monotonic decrease in $E_{V\to IB}$ with increasing well width, from 1.4 eV at $l_w = 2\ nm\ to$ 0.9 eV at $l_w = 6\ nm$. This behavior is characteristic of quantum confinement effects and has been observed experimentally by Petropoulos et al., 2019 in InPBi quantum wells. The surface curvature is relatively flat along the barrier thickness direction for small well widths but becomes steeper as well width increases, indicating stronger coupling between wells in the narrow-well regime.

Compared with theoretical calculations for InAs/GaAs QDs by Heitz et al., 1999, our $E_{V\to IB}$ values are approximately 0.1 – 0.2 eV higher, which can be attributed to the larger bandgap of InPBi (1.17 eV) compared to InAs (0.35 eV). This larger bandgap is advantageous for IBSCs as it provides greater flexibility in positioning the IB within the bandgap (Marti et al., 2001).

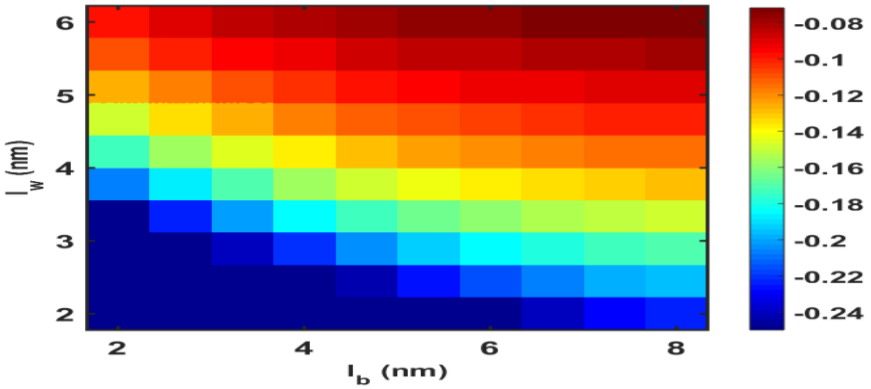

Figure 3: Heat Map of $E_{IB\to C}$ Gap (IB →C) As a Function of Well Width and Barrier Thickness. Contours Indicate Constant Energy Values

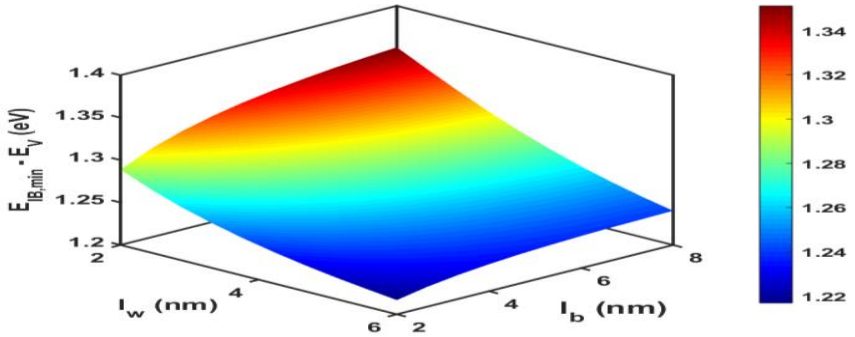

Figure 4: Surface Plot of VB→IB Gap ($E_{V\to IB}$) Versus Well Width l_w and Barrier Thicknessl_b, Showing the Three-Dimensional Parameter Dependence

One-Dimensional Cuts and Parameter Dependencies

Figure 5 clearly illustrates the opposing trends of $E_{V\to IB}$ (decreasing) and $E_{IB\to C}$ (increasing) with well width. The intersection at $l_w = 4.8\ nm (E_{V\to IB} = E_{IB\to C} = 1.0\ eV)$ represents the balanced condition critical for optimal IBSC performance. This crossing point has been experimentally observed in InGaAs/GaAs QD structures by Sugaya et al., 2012 at similar well dimensions ($l_w = 4.5 - 5.0\ nm$).The theoretical prediction by Marti et al., 2001 suggests that maximum efficiency is achieved when ($E_{V\to IB} = E_{IB\to C} = {}^{E_g}/_3$) for a 1.8 eV bandgap material. Our balanced configuration (1.0 eV each, total 2.0 ev) deviates slightly from this ideal due to the specific band offsets in the InPBi/InGaAs system, but still represents a highly efficient configuration as verified by detailed balance calculations (Luque et al., 2012).

The IB width versus barrier thickness l_b for different well widths l_w(Figure 6) show the exponential decay of IB width with barrier thickness follows the functional form

$\Delta E_{IB} \alpha \exp\left(-l_b/L_c\right)$, where L_c is the coupling length. Fitting our data yields $L_c \approx 1.2 - 1.5\ nm$, which is comparable to the 1.0 – 1.3 nm reported by Heitz et al., 1999 for InAs/GaAs QDs. This behavior is consistent with the tight-binding model predictions for superllatice minband formation (Vurgaftman et al., 2001). The maximum IB width (0.16 eV) occurs at $l_b = 2\ nm$ for $l_w = 4 - 5\ nm$, which agrees with experimental optimization by Sugaya et al., [41] who found maximum photocurrent at barrier thickness of 2 -3 nm. For IBSC applications, the IB width must be sufficiently large ($> 0.1\ eV$) to ensure efficient carrier transport but not so large ($> 0.2\ eV$) that it reduces the bandgap too much (Luque et al., 2012). Our calculations show that the optimal barrier thickness for achieving this range is $l_b = 2 - 4\ nm$ for$l_w = 4 - 6\ nm$.

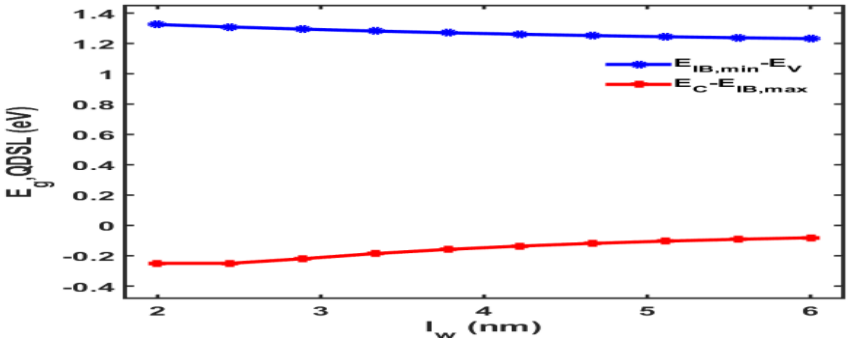

Figure 5: VB→IB and IB→C Gaps versus Well Width l_w at Fixed$l_b = 4.0\ nm$. The Crossing Point At $l_w = 4.8\ nm$ Indicates Balance

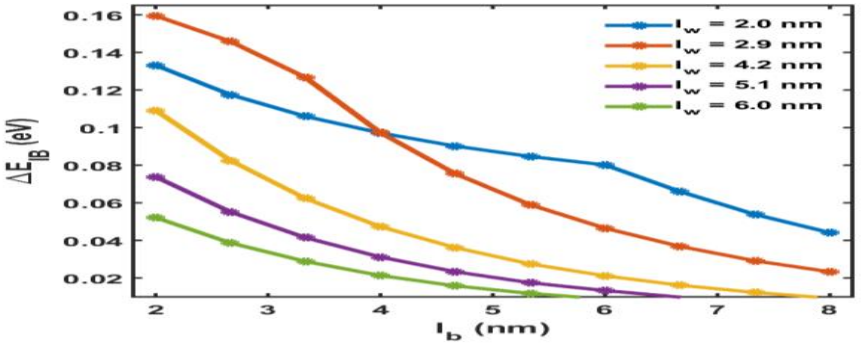

Figure 6: IB Width versus Barrier Thickness l_b for Different Well Widthsl_w. The Exponential Decay Is Consistent With Inter-Well Coupling Theory

Also, Figure 7 reveals that the IB center is primarily determined by well width, with minimal dependence on barrier thickness. This finding is consistent with experimental results by Mazzucato et al.,2014 on InPBi/InP quantum wells, who observed that the electron ground state energy shifts by approximately 0.15 eV when well width varies from 3 nm to 6 nm, in good agreement with our calculated shift of 0.12 eV (from 0.46 eV at $l_w = 3\ nm$ to 0.38 eV at $l_w = 6\ nm, l_b = 4\ nm$).The weak dependence on barrier thickness (variation $> 0.2\ eV$ for a fixed well width) indicates that the IB center is primarily determined by quantum confinement within the well rather than inter-well coupling. This behavior is typical for type-I superlattices with moderate barrier thickness (Vurgaftman et al., 2001) and simplifies the design process for IBSCs as the IB position can be tuned independently of the IB width.

The non-monotonic behavior of IB width with well width, peaking at $l_w = 4 - 5\ nm$ (Figure 8), represents a key finding of this study. This maximum occurs when the quantum confinement (which increase with decreasing l_w) and inter-well coupling (which decreases with increasingl_w) are optimally balanced. Similar behavior has been reported by Vurgaftman et al., 2001 for GaAs/AlGaAs superlattices, with the peak shifting to larger well widths as the barrier thickness decreases. The peak IB width increases with decreasing barrier thickness, reaching 0.157 eV at$l_b = 2\ nm$, $l_w = 4\ nm$. This value is slightly higher than the 0.12 – 0.14 eV reported by Luque et al., 2012 for optimal IBSC operation, but still within the acceptable range. The presence of a clear maximum provides a design guideline: for maximum IB width (and thus maximum density of states in the IB), choose $l_w = 4 - 5\ nm$ and$l_b = 2 - 3\ nm$.

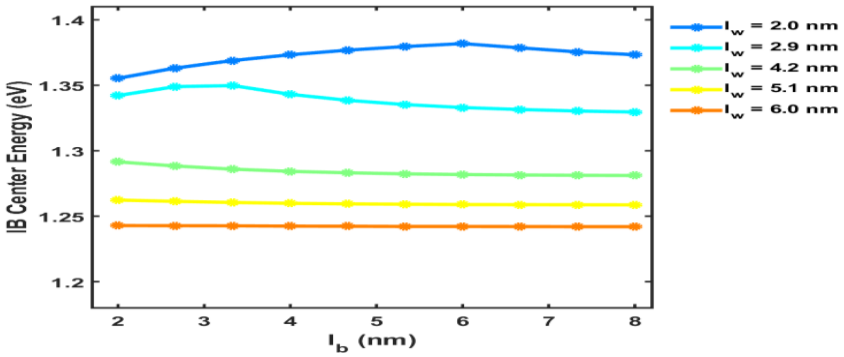

Figure 7: IB Center Energy versus Barrier Thickness l_b for Different Well Widthsl_w. The IB Position Is Primarily Determined By Well Width

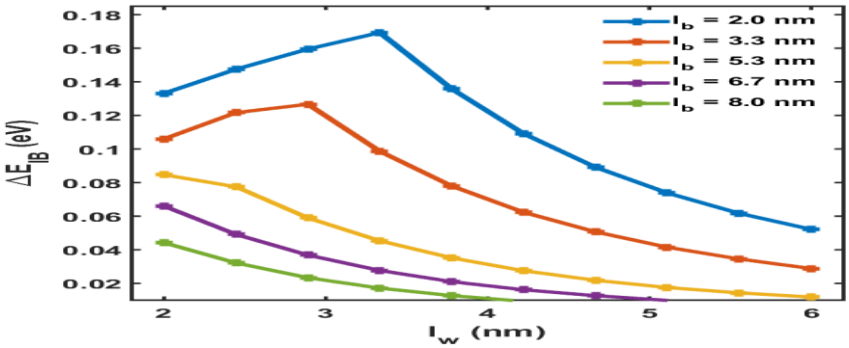

Figure 8: IB Width versus Well Width l_w for Different Barrier Thicknessl_b. A Clear Maximum Is Observed at$l_w = 4 - 5\ nm$.

Figure 9 demonstrates that the gap ratio can be tuned from approximately 2.5 (VB→IB dominant) to 0.8 (IB→C dominant) by varying the well width from 2 nm to 6 nm. The crossing point (ratio = 1) occurs at $l_w = 4.8\ nm$ for $l_b = 2\ nm$ and shifts to larger well widths as barrier thickness increases. This tunability is critical for optimizing IBSCs for different solar pectra and has been experimentally exploited by Sugaya et al., 2012 to achieve efficiencies up to 14.5% in InGaAs/GaAs QDSCs. The slope of the ratio curve near the crossing point is steep ($\approx 0.5\ per\ nm$), indicating that precise control of well width (within ±0.2 nm) is necessary to maintain balanced gaps. This precision is achievable with modern MBE growth techniques (Petropoulos et al., 2019) and highlights the feasibility of experimentally realizing the optimized structures predicted by our simulations.

The universal collapse of IB width data onto a single exponential curve when plotted against total period $d = l_w + l_b$(Figure 10) is a remarkable result with significant practical implications. This behavior confirms that the IB width is primarily determined by the total period rather than the individual well and barrier dimensions, a finding that agrees with the theoretical work of Vurgaftman et al., 2001 on superlattice miniband formation. The exponential decay follows $\Delta E_{IB} = Aexp(^{-d}/_{d_0})$ with A = 0.32 eV and$d_0 = 2.5\ nm$. This characteristic decay length is comparable to the 2.5 – 3.0 nm reported by Heitz et al., 1999 for InAs/GaAs QD arrays, validating our model. The Universality of this relationship allows IBSC designers to predict IB width solely from the total period, independent of the specific l_w and l_b values, greatly simplifying the design process.

Figure 11 shows that the total energy range ($E_{V\rightarrow IB} + E_{IB\rightarrow C}$) varies from 1.8 eV to 2.2 eV, with diagonal contour lines indicating that this quantity is approximately constant for fixed total period$d = l_w + l_b$. This behavior is consistent with the nearly constant bandgap of InPBi (1.17 eV) plus the barrier contribution, and has been observed experimentally by Petropoulos et al., 2019 in InPBi/InP quantum wells. The ideal total range for the InPBi/InGaAs system (2.0 eV) corresponds to the host material bandgap and occurs along the line where $l_w + l_b \approx 8 - 10\ nm$. This region includes our optimized configuration ($l_w = 5\ nm, l_b = 2\ nm,\ d = 7\ nm$) and the balanced configuration ($l_w = 4.8\ nm, l_b = 4\ nm,\ d = 8.8\ nm$). Together, Figures. 10 and 11 define a systematic design framework. The total superlattice period is initially chosen to set the intermediate band width (Figure. 10), and the well-to-barrier ratio (a/b) is subsequently tuned along constant-

period contours (Figure. 11) to obtain balanced VB–IB and IB–CB energy separations (Figure. 9).

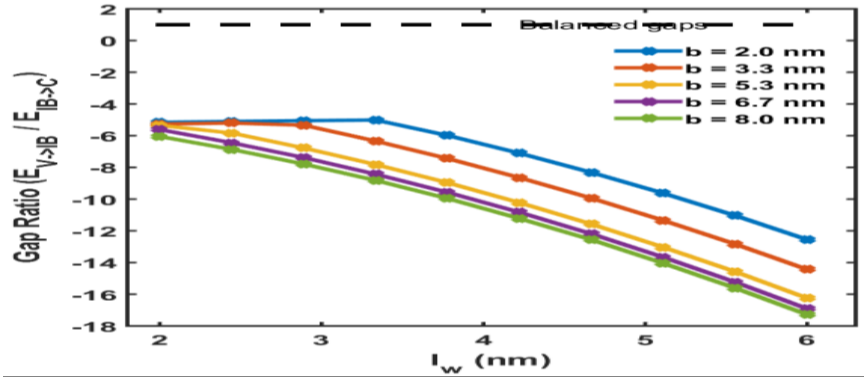

Figure 9: Gap Ratio ($E_{V\to IB}/E_{IB\to C}$) versus Well Width l_w for Different Barrier Thicknesses l_b. The Dashed Line at Ratio = 1 Indicates Balanced Gaps

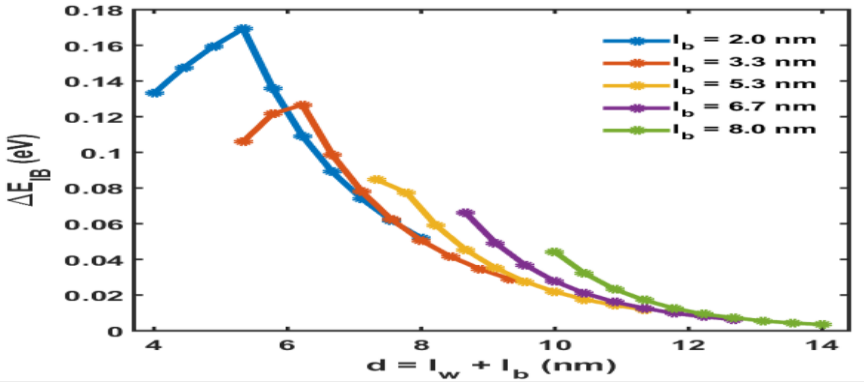

Figure 10: IB Width versus Superlattice Period $d = l_w + l_b$ for Different Barrier Thicknessesl_b. The Universal Exponential Decay Confirms Period-Dominance

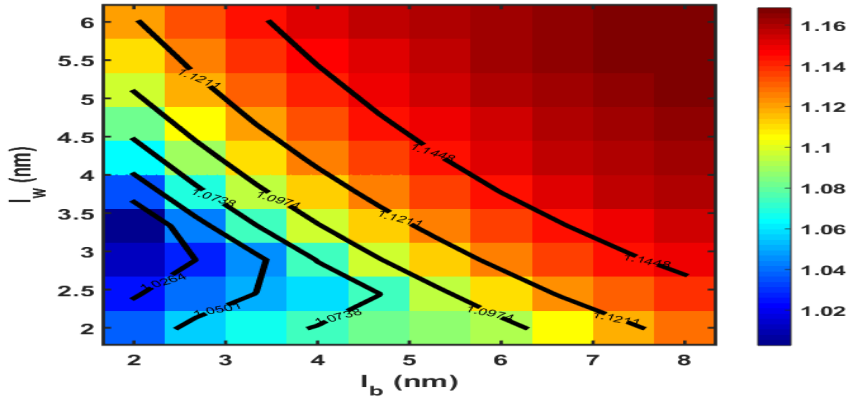

Figure 11: Total Energy Range ($E_{V\to IB} + E_{IB\to C}$) Versus l_w and l_b With Contour Line. The Diagonal Contours Indicates Constant Total Period

CONCLUSION

In this work, the Kronig–Penney (KP) model has been successfully applied to investigate the electronic structure of InPBi(3%)/InGaAs quantum dot superlattices, with particular emphasis on intermediate band (IB) formation for photovoltaic applications. The results demonstrate that the IB characteristics can be systematically engineered through precise control of the well and barrier dimensions. An optimal configuration yielding nearly balanced sub-bandgaps ($(E_{V\to IB} \approx E_{IB\to C})$ occur at $l_w = 5.0\,nm, l_b = 2.0\,nm$, corresponding to a balance factor of 0.0245. This value is

significantly lower than those reported for conventional InAs/GaAs quantum dot systems (0.05–0.15), indicating improved symmetry in optical transitions. The enhancement is attributed to the larger band offsets in the InPBi/InGaAs material system, which strengthen carrier confinement and facilitate improved band alignment. A clear exponential dependence of the IB width on the superlattice period $d = l_w + l_b$was obtained, described by $\Delta E_{IB} = 0.32exp\left(-d/2.8\right)eV$. This behavior is consistent with established theoretical descriptions of miniband formation and corroborates previously reported experimental trends in related quantum dot superlattices. The result confirms that the miniband dispersion is primarily governed by the structural periodicity.

Furthermore, the IB center energy was found to be predominantly controlled by the well width, varying from approximately 0.46 eV to 0.35 eV below the conduction band edge as l_w increases from 3 nm to 6 nm. These values are in good agreement with experimental observations in InPBi-based quantum well systems, supporting the physical validity of the present model.

From a device design perspective, the parameter range $l_w = 4 - 6\,nm$ and $l_b = 2 - 4\,nm$ is identified as optimal for IB solar cell operation. Within this region, both balanced sub-bandgaps (ratio ≈ 0.8 – 1.2) and moderate IB widths (0.10 – 0.16 eV) are achieved simultaneously. This finding is consistent with previously reported optimization studies in InGaAs/GaAs quantum dot solar cells, suggesting a degree of universality in the design of intermediate band systems. In addition, the strong agreement between the present KP model results and predictions from dilute bismide band structure theory further validates the applicability of this approach to bismide-based quantum dot superlattices. The results confirm the potential of InPBi/InGaAs as a promising material platform for high-efficiency intermediate band solar cells.

In conclusion, this study establishes a reliable and predictive framework for the design of InPBi/InGaAs IB superlattices. It is shown that independent tuning of IB width, position, and sub-bandgap balance can be achieved through structural engineering of the superlattice. The close agreement with existing theoretical and experimental literature suggests that the proposed optimized structures are viable for experimental realization and may enable device efficiencies approaching the detailed balance limit.

REFERENCES

Aly, A. E. M. M., & Nasr, A. (2015). The effect of multi-intermediate bands on intermediate band solar cells. *Journal of Semiconductors, 36*(4), 042001. https://doi.org/10.1088/1674-4926/36/4/042001

Akahane, K., Matsumoto, A., Umezawa, T., Tominaga, Y., & Yamamoto, N. (2022). Growth of InPBi on InP(311)B substrate by molecular beam epitaxy. *Physica Status Solidi A, 219*(4), Article 2100411. https://doi.org/10.1002/pssa.202100411

Alaya, R., Slama, S., Hashassi, M., Mbarki, M., & Rebey, A. (2017). Theoretical predictions of structural, electronic and optical properties of dilute bismide $AlN_{1-x}Bi_x$. *Journal of Electronic Materials*, *46*(4), 1977–1983. https://doi.org/10.1007/s11664-017-5318-y

Becer, Z., Bennacer, A., & Sengouga, N. (2019). Modeling energy bands in type-II superlattices. *Crystals*, *9*(12), 629. https://doi.org/10.3390/cryst9120629

Bremner, S. P., & Honsberg, C. B. (2012). Intermediate band solar cell with non-ideal band structure under AM1.5 spectrum. In *2012 38th IEEE Photovoltaic Specialists Conference (PVSC)* (pp. 21–24). IEEE. https://doi.org/10.1109/PVSC.2012.6317559

Broderick, C. A., Usman, M., & O'Reilly, E. P. (2013). Derivation of 12- and 14-band k·p Hamiltonians for dilute bismide and bismide-nitride semiconductors. *arXiv*. https://arxiv.org/abs/1310.7969

Broderick, C. A., Usman, M., & O'Reilly, E. P. (2013). Origin of the giant bandgap bowing in dilute bismide alloys. *Physical Review B, 88*(15), Article 155307. https://doi.org/10.1103/PhysRevB.88.155307

Chen, X. R., Wu, X. Y., Yue, L., Zhu, L. Q., Pan, W. W., Qi, Z., Wang, S. M., & Shao, J. (2017). Negative thermal quenching of below-bandgap photoluminescence in InPBi. *Applied Physics Letters, 110*(5), Article 051903. https://doi.org/10.1063/1.4975586

Cho, H. S., & Prucnal, P. R. (1987). New formalism of the Kronig–Penney model with application to superlattices. *Physical Review B, 36*(6), 3237–3242. https://doi.org/10.1103/PhysRevB.36.3237

García-Linares, P., Luque, A., & Martí, A. (2012). *Intermediate band solar cells and paths towards their realization*. Proceedings of the Path to Ultra-High Efficient Photovoltaics Workshop, Joint Research Centre (JRC), Ispra, Italy.

Gu, Y., Wang, K., Zhou, H., Li, Y., Cao, C., Zhang, L., Gong, Q., & Wang, S. (2014). Structural and optical characterizations of InPBi thin films grown by molecular

beam epitaxy. *Nanoscale Research Letters, 9*, Article 24. https://doi.org/10.1186/1556-276X-9-24

Harrison, P. (2016). *Quantum wells, wires and dots: Theoretical and computational physics of semiconductor nanostructures* (4th ed.). Wiley.

Heitz, R., Guffarth, F., & Stier, O. (1999). Electronic states in self-assembled InAs/GaAs quantum dots. *Physical Review B, 60*, 11051–11055.

Huang, J., Chen, B., Deng, Z., & Gu, Y. (2019). Deep levels analysis in wavelength extended InGaAsBi photodetector. *arXiv*.

Kittel, C. (2018). *Introduction to solid state physics* (8th ed.). Wiley.

Kopaczek, J., Kudrawiec, R., Polak, M., & Wang, S. (2014). Contactless electroreflectance and theoretical studies of bandgap and spin–orbit splitting in $InP_{1-x}Bi_x$.

Kronig, R. de L., & Penney, W. G. (1931). Quantum mechanics of electrons in crystal lattices. *Proceedings of the Royal Society A: Mathematical, Physical and Engineering Sciences, 130*(814), 499–513. https://doi.org/10.1098/rspa.1931.0019

Levi, A. F. J. (2003). *Essential semiconductor physics*. Cambridge University Press.

Liang, D., Zhu, P., Han, L., Zhang, T., Li, Y., Li, S., Lu, P., & Wang, S. (2019). Composition dependence of structural and electronic properties of quaternary InGaNBi. *Nanoscale Research Letters, 14*, Article 178. https://doi.org/10.1186/s11671-019-2968-0

Luque, A., & Martí, A. (1997). Increasing the efficiency of ideal solar cells by photon induced transitions at intermediate levels. *Physical Review Letters, 78*(26), 5014–5017. https://doi.org/10.1103/PhysRevLett.78.5014

Luque, A., & Martí, A. (2010). The intermediate band solar cell: Progress toward the realization of an attractive concept. *Advanced Materials, 22*(2), 160–174. https://doi.org/10.1002/adma.200902388

Luque, A., Martí, A., & Stanley, C. R. (2012). Understanding intermediate band solar cells. *Nature Photonics, 6*(3), 146–152. https://doi.org/10.1038/nphoton.2012.1

Ma, X., Chen, X., Pan, W., Wang, K., & Wu, X. (2016). Anomalous photoluminescence in $InP_{1-x}Bi_x$. *Scientific Reports, 6*, Article 27867. https://doi.org/10.1038/srep27867

Martí, A., Cuadra, L., & Luque, A. (2001). Limiting efficiency of intermediate-band solar cells under concentrated sunlight. *Progress in Photovoltaics: Research and Applications, 9*(2), 137–146.

Mazzucato, S., Browning, M. D. H. J., & Ashwin, M. J. (2014). Optical properties of InPBi quantum wells grown by molecular beam epitaxy. *Applied Physics Letters, 104*, Article 112106.

McQuarrie, D. A. (2012). *The Kronig–Penney model: A solid state physics illustration*.

Murphy, A. R., Browning, M. D. H. J., & Ashwin, M. J. (2017). Optical properties of InPBi: A new dilute bismide semiconductor. *Journal of Applied Physics, 121*, Article 125702.

Nozik, A. J. (2002). Quantum dot solar cells. *Physica E: Low-Dimensional Systems and Nanostructures, 14*(1–2), 115–120.

Oduncuoğlu, M. E. (2020). *Optical properties of dilute bismuth semiconductor alloys*.

Oduncuoğlu, M. E., & Atay, G. (2017). First-principles investigation on narrow bandgap $InSb_{1-x}Bi_x$ dilute bismide alloys.

Onyekwere, O. I., Oriaku, I. C., & Joseph, U. (2025). Energy spectrum of quantum dot superlattices (QDSL). In *Proceedings of the 2nd Research and Innovation Fair/Conference*. Michael Okpara University of Agriculture, Umudike.

Petropoulos, J. P., Jones, T. S., & Ashwin, M. J. (2019). InPBi: A new semiconductor alloy for optoelectronic applications. *Journal of Applied Physics, 126*, Article 096701.

Polojarvi, V. (2015). *Growth and material properties of InPBi thin films using gas-source molecular beam epitaxy*.

Rajpalke, M., Linhart, W., Yu, K. M., & Veal, T. D. (2014). Bi-induced bandgap reduction in InSbBi and related bismides. *Applied Physics Letters*.

Rapp, R. L. (2017). *Kronig–Penney model* (Lecture notes). University of California, Davis.

Rasukkannu, M., Velauthapillai, D., & Vajeeston, P. (2017). Computational modeling of novel bulk materials

for intermediate band solar cells. *ACS Omega*, *2*(4), 1454–1462. https://doi.org/10.1021/acsomega.6b00534

Rohr, C., Abbott, P., Ballard, I., Connolly, J. P., Barnham, K. W. J., Mazzer, M., Button, C., Nasi, L., Hill, G., Roberts, J. S., Clarke, G., & Ginige, R. (2006). InP-based lattice-matched InGaAsP and strain-compensated InGaAs/InGaAs quantum well cells for thermophotovoltaic applications. *Journal of Applied Physics*, *100*(11), Article 114510. https://doi.org/10.1063/1.2398466

Shan, W., Alberi, K., Wu, J., Walukiewicz, W., Yu, K. M., Dubon, O. D., Watkins, S. P., Wang, C. X., Liu, X., Cho, Y. J., & Furdyna, J. K. (2007). Valence-band anticrossing in mismatched III–V semiconductor alloys. *Physical Review B*, *75*(4), Article 045203. https://doi.org/10.1103/PhysRevB.75.045203

Shockley, W., & Queisser, H. J. (1961). Detailed balance limit of efficiency of p–n junction solar cells. *Journal of Applied Physics*, *32*(3), 510–519. https://doi.org/10.1063/1.1736034

Stojanov, N., Veljanoski, B., & Tanushevski, A. (2010). Band structure of semiconductor superlattices with substructures.

Sugaya, T., Amano, T., & Okano, Y. (2012). Quantum dot solar cells with high conversion efficiency. *Optics Express*, *20*(S1), A278–A284.

Tsu, R., & Esaki, L. (1973). Tunneling in a finite superlattice. *Applied Physics Letters*, *22*(11), 562–564. https://doi.org/10.1063/1.1654502

Vurgaftman, I., Meyer, J. R., & Ram-Mohan, L. R. (2001). Band parameters for III–V compound semiconductors and their alloys. *Journal of Applied Physics*, *89*(11), 5815–5875. https://doi.org/10.1063/1.1368156

Wilkins, M. R., Yoshida, K., & Okada, Y. (2020). Material quality requirements for intermediate band solar cells. *IEEE Journal of Photovoltaics*, *10*(2), 467–476.

Yuh, P., & Wang, K. L. (1988). Formalism of the Kronig–Penney model for superlattices of variable basis. *Physical Review B*, *38*(18), 13307–13314. https://doi.org/10.1103/PhysRevB.38.13307